NASA/TM–20240014376

An Experimental and Predictive Study of Bent-Chamber Acoustic Liners

Jordan Kreitzman
Langley Research Center, Hampton, Virginia, 23681-2199

Michael G. Jones
Langley Research Center, Hampton, Virginia, 23681-2199

November 2024

NASA STI Program Report Series

Since its founding, NASA has been dedicated to the advancement of aeronautics and space science. The NASA scientific and technical information (STI) program plays a key part in helping NASA maintain this important role.

The NASA STI Program operates under the auspices of the Agency Chief Information Officer. It collects, organizes, provides for archiving, and disseminates NASA's STI. The NASA STI Program provides access to the NASA Aeronautics and Space Database and its public interface, the NASA Technical Report Server, thus providing one of the largest collection of aeronautical and space science STI in the world. Results are published in both non-NASA channels and by NASA in the NASA STI Report Series, which includes the following report types:

- TECHNICAL PUBLICATION. Reports of completed research or a major significant phase of research that present the results of NASA programs and include extensive data or theoretical analysis. Includes compilations of significant scientific and technical data and information deemed to be of continuing reference value. NASA counterpart of peer-reviewed formal professional papers, but having less stringent limitations on manuscript length and extent of graphic presentations.
- TECHNICAL MEMORANDUM. Scientific and technical findings that are preliminary or of specialized interest, e.g., quick release reports, working papers, and bibliographies that contain minimal annotation. Does not contain extensive analysis.
- CONTRACTOR REPORT. Scientific and technical findings by NASA-sponsored contractors and grantees.
- CONFERENCE PUBLICATION. Collected papers from scientific and technical conferences, symposia, seminars, or other meetings sponsored or co-sponsored by NASA.
- SPECIAL PUBLICATION. Scientific, technical, or historical information from NASA programs, projects, and missions, often concerned with subjects having substantial public interest.
- TECHNICAL TRANSLATION. English-language translations of foreign scientific and technical material pertinent to NASA's mission.

Specialized services also include organizing and publishing research results, distributing specialized research announcements and feeds, providing information desk and personal search support, and enabling data exchange services.

For more information about the NASA STI Program, see the following:

- Access the NASA STI program home page at `http://www.sti.nasa.gov`
- E-mail your question to `help@sti.nasa.gov`
- Phone the NASA STI Information Desk at 757-864-9658
- Write to:
  NASA STI Information Desk
  Mail Stop 148
  NASA Langley Research Center
  Hampton, VA 23681-2199

NASA/TM–20240014376

An Experimental and Predictive Study of Bent-Chamber Acoustic Liners

Jordan Kreitzman
Langley Research Center, Hampton, Virginia, 23681-2199

Michael G. Jones
Langley Research Center, Hampton, Virginia, 23681-2199

National Aeronautics and
Space Administration

Langley Research Center
Hampton, Virginia 23681-2199

November 2024

Acknowledgments

This work was conducted in support of the Advanced Air Transport Technology (AATT) Project of the NASA Advanced Air Vehicle Program (AAVP). The authors wish to thank Mr. Robert Andrews for both creating the sample drawings as well as printing the samples. Additionally, the authors express gratitude to both Dr. Alexander Carr and Dr. Travis Turner for thorough reviews of the document.

Available from:

NASA STI Program / Mail Stop 148
NASA Langley Research Center
Hampton, VA 23681-2199
Fax: 757-864-6500

Abstract

Acoustic liner samples with rectangular, sharp chamber bends are 3D-printed and tested in the NASA Normal Incidence Tube. The angle of the bend is varied from 0° to 180°. Four different methods are used to predict the impedance behavior of these samples: (1) midline-length assumption, (2) Cummings correction for curved duct bends, (3) Cummings prediction for 180° sharp duct bends, and (4) Helmholtz equation via finite element method. Trends in the experimental data are discussed, predictions are compared to the experimental data, and recommendations are made on prediction method usage. Follow-on work is suggested, including capturing additional test points at higher frequencies and with different chamber geometries. Future modeling strategies are also briefly described.

Nomenclature

Symbols	**Description**
β, β_i	admittance for entire sample and for the i^{th} chamber
c, ρ	sound speed and density of air
δ_i	total mass-end correction value of i^{th} chamber
δ_{ij}	mass-end correction value of i^{th} chamber due to j^{th} chamber
$G_{m/n}, H_{m/n}, H'_{m/n}$	radiation impedance intermediate calculations
Γ_m	term used in acoustic modal solution, dependent on mode number
$i, \Im\{\}$	imaginary number ($\sqrt{-1}$) and imaginary portion of value
J'_q, Y'_q	Bessel function derivatives of first and second kind with order q
k, k_ϕ, ω, t	free-space and angular wavenumbers, angular frequency, and time
$k_{i,m}$	axial wavenumber for mode m and i^{th} section of a chamber
l_c, l_m, t_p	chamber side and midline lengths, partition thickness between chambers
l_1, l_2, b	straight chamber lengths and slot height used in prediction analyses
m, n	mode orders for rectangular duct
N_c	number of open chambers on the surface of the sample
Ω	ratio of acoustically active surface area to total surface area of liner
p_1, p_2, p_3	acoustic pressures for three sections in a chamber
$P^{\pm}_{i,m}$	incident/reflected ($\pm$) modal (m) amplitudes for i^{th} section of a chamber
r_i, r_o, ψ	inner and outer radii of curved duct bend, chamber bend angle (radians)
R, s	reflection coefficient and integer value used during prediction process
w, v_{mn}	radiation impedance intermediate calculations
x_{ci}, y_{ci}	center coordinates of an open chamber surface within the impedance tube
x_t, y_t	impedance tube width and height
ζ_i, χ_c	i^{th} chamber surface impedance and chamber reactance, ρc normalization
ζ, θ, χ	liner surface impedance, resistance, and reactance, ρc normalization

1 Introduction

Modern aircraft engine nacelles are trending towards higher bypass ratios, which consequently lowers the dominant fan noise frequencies. Longer chamber depths are then needed for the integrated acoustic liners to effectively attenuate the fan noise. Since space for the acoustic liner continues to be limited, bending the acoustic liner chambers at various angles for efficient volume usage is a viable option for improved lower-frequency attenuation. It is critical to accurately model these bend effects to ensure future designs are targeting the proper frequencies. A chamber bend can either be curved or sharp, and this is shown in Fig. 1. If a sharp bend is 180°, one can also define a slot height (b), which is the minimum distance from the end of the partition to the back of the chamber.

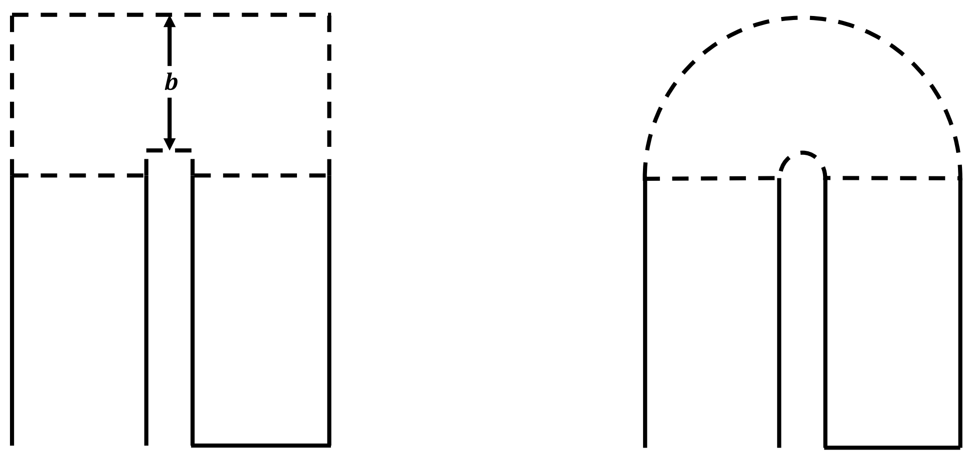

(a) Sharp bend

(b) Curved bend

Figure 1: Chamber bend types with bend sections shown with a dashed line and the slot height denoted as b.

The theory of sound propagation within chamber bends has been looked at previously, although work has mostly excluded sharp bends. Rostafinski [1] provides a detailed summary of numerous works on curved chamber bends. Cummings [2] computed a correction in the impedance calculation for a chamber with a curved bend. He followed this up the subsequent year with formulations that can be used to solve for the surface impedance of 180° sharp bends, both with rectangular and circular annulus cross-sections [3, 4].

Chamber bends have been used successfully in the past to mitigate low-frequency noise in a flow environment. Sawdy & Beckemeyer [5] presented an extended-reaction analysis to predict the behavior of a folded-chamber lining the walls of a circular duct. Yu & Chien [6] and Martinez [7] designed and tested a folded-chamber acoustic liner design for use in the center plug of a commercial aircraft engine nacelle to reduce low-frequency combustor noise. The folded-chamber design replicated the volume of a straight chamber designed for the frequencies of interest. Testing showed significant combustor noise mitigation due to the folded-chamber design. More recently, Nark & Jones [8] tested a bent-chamber liner embedded within a simplified engine bifurcation geometry in the NASA Curved Duct Test Rig. The reactance correction provided in Cummings [2] was used to model the impedance, and this was subsequently used as a boundary condition within an approximated convected Helmholtz equation solver for design and prediction purposes. This was followed up by Nark et al. [9], which designed small diameter bent-chamber acoustic liners to maximize volume usage in a highly limited space within an engine nacelle. These particular designs in Nark et al. [9] may be tested in a static engine environment in the near future.

There have been numerous studies on bent-chamber liners within the normal-incidence environment as well. Parrott et al. [10] and Howerton & Parrott [11] analyzed skewed resonator configurations, where the chambers are narrow and bend sharply up to 180°. It was found that modeling the skewed resonators as straight resonators of an equivalent midline length was satisfactory for modeling purposes, although it should be noted that the nondimensional frequencies (kl_c) were quite low for these samples. The success of the simplified model is due to the fact that the propagating waves in a bend behave largely in a one-dimensional manner when the frequency or chamber diameter is small enough. Some recent research has also successfully used a midline-length assumption for bent chambers and perforates [9, 12], but again, the kl_c values were low. Sugimoto et al. [13] assessed 90° bent-chamber liners computationally through Actran TM [14]. They determined that a 90° bent-chamber liner impedance aligned reasonably well at low frequencies with the impedance prediction of a straight chamber with an equivalent midline length. As the frequency went up, the 90° bent-chamber gradually became more similar in impedance to an assumed straight chamber depth equivalent to that of the length from the liner surface to the wall of the bend. This further supports the notion that as kl_c increases, using a midline-length assumption for the impedance prediction is not adequate.

Marinova et al. [15] developed a code to efficiently pack bent chambers in a given volume to maximize space usage. Chambers et al. [16] assessed numerous different bend types as an attempt to maximize low-frequency absorption. This included chambers with multiple bends as well as spiral-shaped chambers. These samples were tested in a normal-incidence impedance tube, and impedance predictions were made with a midline-length assumption. Excellent low-frequency absorption was obtained. Palani et al. [17] analyzed variable-depth, bent-chamber liners with embedded septa for both low-frequency and broadband performance. Jones et al. [18] utilized the slots needed for water drainage in engine nacelle honeycomb core to create a bent-chamber. The work provided in Cummings [2] was used to complement the impedance predictions in Jones et al. [18], and it was found that varying the height of the slot was a significant tuning parameter that should be explored further.

More recently, extensions to the bent-chamber concept have been applied to other aspects of an acoustic liner. Jones et al. [19] shows the ONERA long elastic open neck acoustic resonator (LEONAR) concept. Here the perforations in the facesheet are extended into the chamber, and it is shown that these extensions can be straight, spiraled, etc. Kreitzman [12] also took the bent-chamber idea and applied it to perforations in a facesheet. In that study, the perforations are bent at two 90° angles to support efficient packing in a standard thickness facesheet.

It is clear that numerous researchers and engineers over the years have used the bent-chamber concept successfully. However, work pertaining to improved impedance prediction of these concepts has remained limited. The intent of the current paper is to assess a number of bent-chamber liner samples, both experimentally and analytically. These samples are meant to assess the impedance characteristics when the midline lengths are kept nearly constant, but the bend angle changes. This helps evaluate the accuracy of a midline-length assumption model. Additionally, other samples are created that both vary the slot height and the straight chamber lengths that connect to the bend. Four different impedance modeling strategies are assessed: (1) midline-length assumption, (2) Cummings correction for curved duct bends, (3) Cummings prediction for 180° sharp duct bends, and (4) Helmholtz equation via finite element method. In doing so, one can verify the accuracy of certain models (via comparisons to experimental data) that numerous researchers have used over the years to predict bent-chamber acoustic liners.

The remaining sections of the paper are as follows. A brief description of the test rig and experimental setpoints is provided in Sec. 2. This is followed by a detailed description of the test samples themselves in Sec. 3. After this, Sec. 4 shows the impedance prediction theory behind all four methods. In Sec. 5, trends and observations in the experimental data are discussed, and comparisons to predictions are provided in Sec. 6. Finally in Sec. 7, a detailed summary of all findings is provided followed by future work that needs to take place to confirm the findings suggested in this paper.

2 Normal Incidence Tube (NIT) Test Rig

The NASA Normal Incidence Tube (NIT) is a $2'' \times 2''$ waveguide of approximately $36''$ in length and shown in Fig. 2. It uses six BMS Speaker 4599ND $2''$ compression acoustic drivers to generate a sound field that impinges on the acoustic liner surface. There are three flush, wall-mounted microphones associated with the rig. One is a reference microphone $0.25''$ away from the sample surface that is used to provide feedback in setting the appropriate total sound pressure level (SPL) (incident plus reflected) for the test. Two other microphones, located $2.50''$ and $3.75''$ from the liner surface, are mounted in a rotating plug so that their positions can be interchanged [20]. This allows errors associated with the amplitudes and phases due to mismatched microphone calibrations to be eliminated during the two-microphone method process [21, 22].

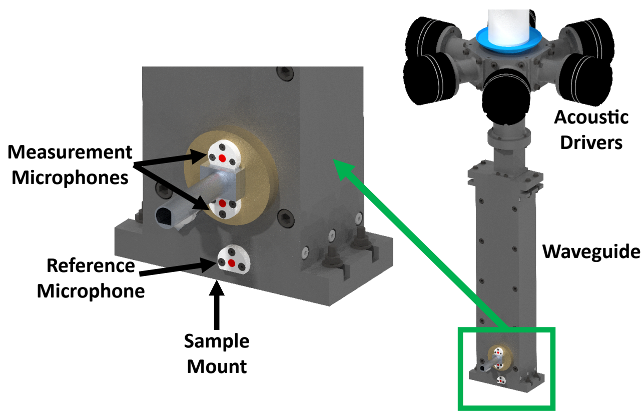

Figure 2: Normal Incidence Tube (NIT) test rig [Source: NASA].

The NIT allows for four different source types: stepped-sine, swept-sine, broadband, and multitone at frequencies of 400–3000 Hz [20, 23]. The highest frequency tested in the NIT is kept sufficiently low so that only plane waves propagate within the waveguide. For this particular test, the swept-sine source is used at SPL levels of 120 and 140 dB. For computing the impedance, the multi-point method is used [22, 24], which uses a weighted residual technique to minimize the error between measured data and an assumed one-dimensional standing wave pattern. Note that when only two microphones are used, this method becomes deterministic, and the error between measured and predicted data is zero. With regards to uncertainty, the 95% confidence intervals on the NIT normalized impedance spectra should be less than 0.02 and 0.04 for SPL values of 120 and 140 dB, respectively, at least for the samples considered in this study [25].

3 Sample Geometries

A typical NIT sample consists of a 5×5 array of 0.3″×0.3″ square chambers, separated by 0.1″ thick partitions. This sample setup is typically selected for modeling purposes as well as increased resistance from the chamber walls. However, for this particular test, in order to prevent the chamber bends from interfering with one another, the standard array needs to be modified slightly. For these samples, every other chamber surface is now open to allow sufficient space for the bends, noting that the chambers are still 0.3″×0.3″ square cross-sections. It is also important to note that these samples contain no facesheet to more easily assess the characteristics of the chambers themselves. There are two bend layouts used, shown in Fig. 3. Bend directions are denoted with an arrow. The orange squares represent the chamber surfaces that are open, while the blue squares represent closed surfaces. Bend layout 2 is only used for the 180° chamber-bend samples.

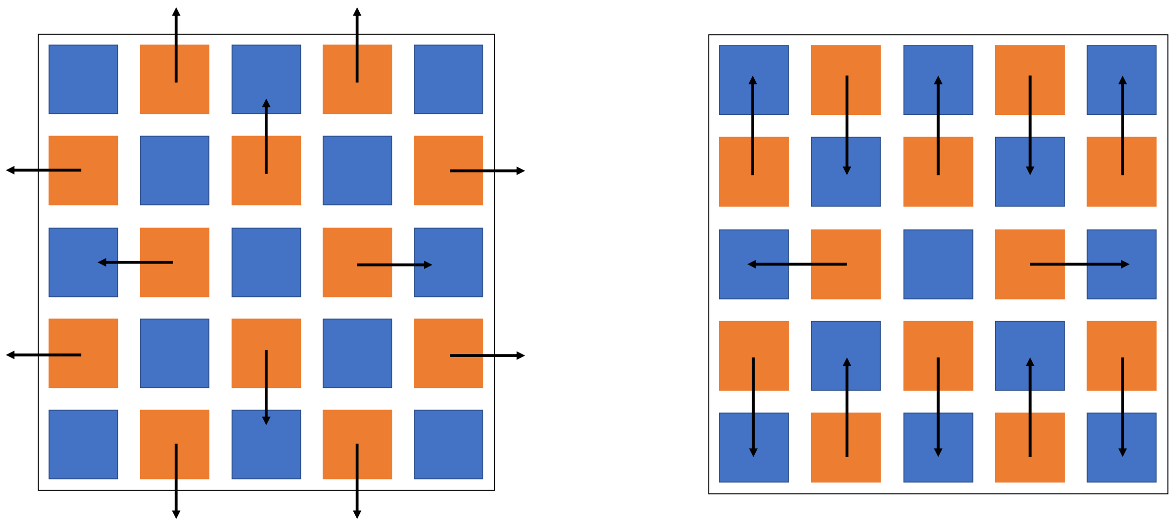

(a) Bend layout 1

(b) Bend layout 2

Figure 3: Bend layouts showing the direction of bends with an arrow. Orange squares indicate open chamber surfaces; blue squares indicate closed surfaces.

The sample names and geometry for each are displayed in Table 1. Please note that samples BC-1 through BC-8 are all designed to have the same total midline length of 2.00″ but differing bend angles. Since the 180° bends must bend back toward the liner surface, there exists a 0.03″ backplate layer, and hence BC-9 has a total midline length that is slightly smaller than BC-1 through BC-8. Additionally, the varying slot heights of BC-10 and BC-11 modify the chamber midline lengths as well. The component midline lengths defined in Table 1 represent the chamber midline segments that are separated by bends, hence why BC-1 only has one component midline length. These component midline lengths are in order of closest to furthest from the liner surface (assuming the total midline lengths are "unwrapped" to be straight). Figure 4 shows an example of the midline-length breakdown for BC-5.

The geometric differences for each sample may be observed in Fig. 5. It is important to note the variation in samples BC-5 and BC-6, where although the total midline lengths are the same

Table 1: Acoustic liner geometries.

Sample Name	Total Midline Length (in.)	Component Midline Lengths (in.)	Bend Angle (degrees)	Slot Height (in.)
BC-1	2.000	2.000	0	N/A
BC-2	2.000	1.000, 1.000	30	N/A
BC-3	2.000	1.000, 1.000	60	N/A
BC-4	2.000	1.000, 1.000	90	N/A
BC-5	2.000	1.250, 0.750	90	N/A
BC-6	2.000	0.750, 1.250	90	N/A
BC-7	2.000	0.855, 0.290, 0.855	120	N/A
BC-8	2.000	0.832, 0.336, 0.832	150	N/A
BC-9	1.970	0.800, 0.400, 0.770	180	0.300
BC-10	1.770	0.700, 0.400, 0.670	180	0.500
BC-11	2.120	0.875, 0.400, 0.845	180	0.150

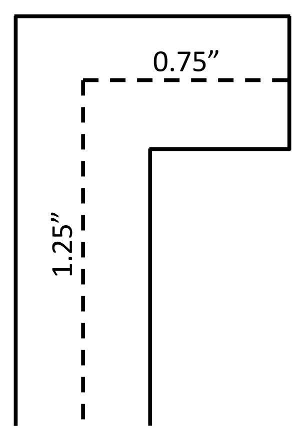

Figure 4: Component midline length diagram for sample BC-5.

between the two, the long and short ends of the chambers are reversed. This is evident from the component midline lengths in Table 1 as well. Additionally, one may see that a surface offset is added to samples BC-7 and BC-8. Due to the bending of the chambers back towards the liner surface, the samples would not be able to fit within the NIT mounting sleeve without an offset added. This offset is simply measured and applied in the post-processing to accurately compute the impedance.

Once the samples exceed a bend angle of 90°, the chambers always have a 0.1″ straight section to transition the bend. This is meant to replicate the partition thickness of the sample. This straight section is included in the midline length calculation. It is important to note that chamber bends greater than 90° without this transition section (i.e., the chamber bends back sharply instead) are not considered in this study but should be assessed in the future.

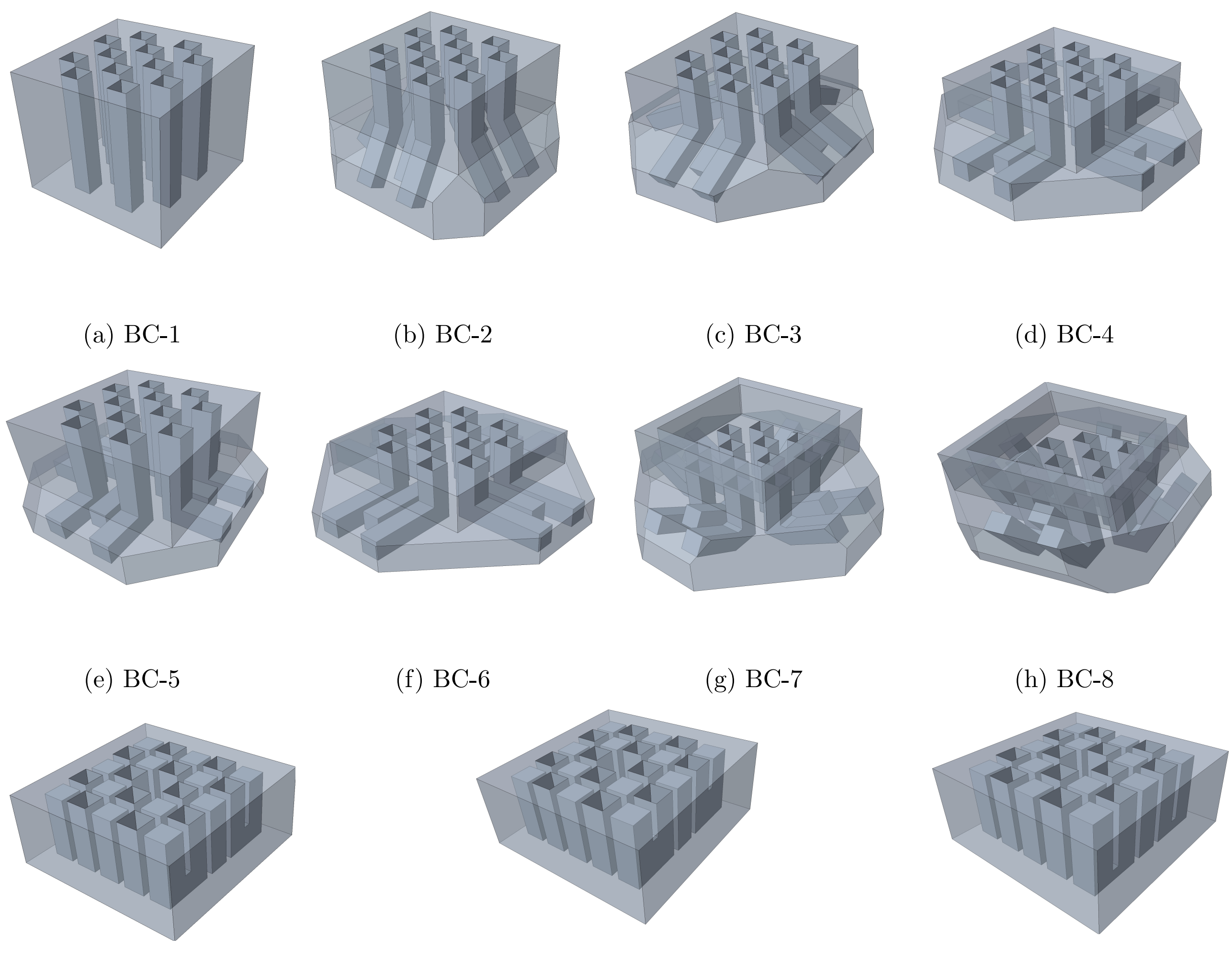

(a) BC-1 (b) BC-2 (c) BC-3 (d) BC-4

(e) BC-5 (f) BC-6 (g) BC-7 (h) BC-8

(i) BC-9 (j) BC-10 (k) BC-11

Figure 5: Acoustic liner geometries.

4 Impedance Prediction Theory

Details regarding the impedance prediction of the samples will be shown for each method in the following sections. The acoustic impedance of each sample is defined as

$$\zeta = \theta + i\chi \approx i\chi, \tag{1}$$

where the $e^{i\omega t}$ convention is used. This relation is assumed to be normalized by the characteristic impedance of air, ρc. Due to the cross-sectional size of the chambers for each sample ($0.3'' \times 0.3''$), it is assumed for this study that there are negligible dissipative losses associated with the chamber walls. Coupled with the fact that there are no facesheets present, the acoustic liner resistance is close to zero as shown in Eq. (1).

As mentioned in the previous section, every other chamber is open at the surface for a given sample due to extra space needed for the chamber bends. Every open chamber radiates noise into the impedance tube, and when these open chambers are more isolated (or tuned to different frequencies), radiation impedance must be accounted for in the overall prediction process [26]. The impedance for a single chamber can be defined as

$$\zeta_i = i(\chi_c + k\delta_i), \tag{2}$$

where a mass-end correction value, δ_i, is used to account for the radiation impedance. Note that the admittance of a single chamber is then defined as $\beta_i = \zeta_i^{-1}$. The details for calculating the mass-end correction term are provided in Sec. 4.1.

The samples in this study are composed of twelve open chambers, each with their own radiation impedance behavior (although some chambers have identical behavior to one another for these samples). Additionally, all closed surfaces and partitions between the chambers must be accounted for in the prediction process. Therefore, one must combine the impedances of the individual open chambers with the rigid surfaces to predict an effective impedance of the entire sample. This can be accomplished via a weighted summation of admittances, shown as

$$\beta = \frac{\Omega}{N_c}\sum_{i=1}^{N_c}\beta_i, \tag{3}$$

where the final impedance of the sample is then simply calculated as $\zeta = \beta^{-1}$.

4.1 Radiation Impedance

The radiation impedance for each open chamber may be calculated by solving for the mass-end correction value, utilizing research originally conducted by Ingard [27] and expanded upon by Ih [28]. Here it is assumed that the chamber radiates noise into the impedance tube like a rectangular piston into an infinitely long rectangular tube. Each chamber experiences self-radiation effects (due to the pressure field it creates acting on itself – this includes effects due to the impedance tube walls) as well as mutual-radiation effects (due to the pressure field of every other chamber acting on the chamber of interest). Ih [28] developed a low-frequency approximation for the mass-end correction term of one rectangular piston due to the radiated noise of another rectangular piston, within an infinitely long rectangular tube. This is shown below as

$$\delta_{ij} = \frac{l_c^2}{\pi x_t y_t}\left(\sum_{m=1}^{\infty}\frac{x_t}{m v_{m0}}G_m^2 H_m H_m' + \sum_{n=1}^{\infty}\frac{y_t}{n v_{0n}}G_n^2 H_n H_n' + \sum_{m=1}^{\infty}\sum_{n=1}^{\infty}\frac{1}{w v_{mn}}G_m^2 G_n^2 H_m H_m' H_n H_n'\right), \tag{4}$$

where $v_{m0} = v_{0n} = 0.5$ and $v_{mn} = 0.25$, and the w term is defined as

$$w = \sqrt{\left(\frac{m}{x_t}\right)^2 + \left(\frac{n}{y_t}\right)^2}. \tag{5}$$

The G_m and G_n terms are defined as

$$G_m = \frac{\sin\left(\frac{m\pi l_c}{2x_t}\right)}{\frac{m\pi l_c}{2x_t}}, G_n = \frac{\sin\left(\frac{n\pi l_c}{2y_t}\right)}{\frac{n\pi l_c}{2y_t}}, \tag{6}$$

while the H_m, H_n, H'_m, and H'_n terms are defined as

$$H_m = \cos\left(\frac{m\pi x_{ci}}{x_t}\right), H_n = \cos\left(\frac{n\pi y_{ci}}{y_t}\right), H'_m = \cos\left(\frac{m\pi x_{cj}}{x_t}\right), \text{ and } H'_n = \cos\left(\frac{n\pi y_{cj}}{y_t}\right). \tag{7}$$

Figure 6 shows the problem setup and coordinate system for the radiation impedance calculation. Note that if one wants to calculate the mass-end correction term of a rectangular piston acting on itself (self-radiation effect), one must simply set the coordinates of the two pistons to be equal, i.e., $(x_{ci}, y_{ci}) = (x_{cj}, y_{cj})$.

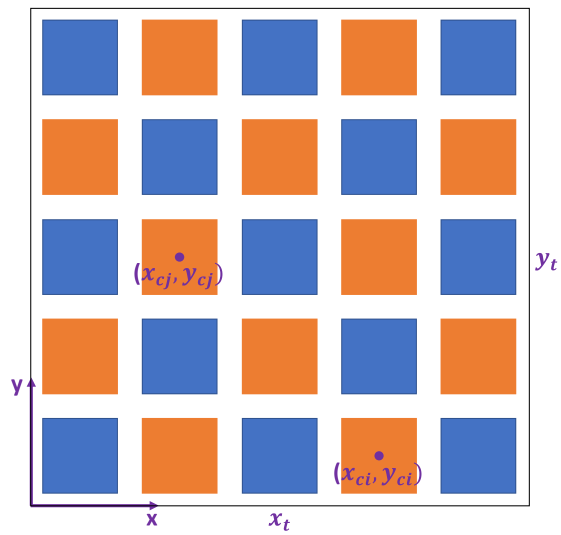

Figure 6: Problem setup and coordinate system for the radiation impedance calculation. The outer square denotes the impedance tube walls.

Equations (4)–(7) are found by assuming linear acoustics and solving for the acoustic potential field due to each piston's motion, noting also that the cross-sectional particle velocity distribution at each piston surface is uniform at low frequencies. The formulation is specifically for two pistons but can easily be extended to multiple pistons. Pritchard [29] notes that the radiation impedance of a piston is the summation of its self-radiation impedance and its mutual radiation impedance with every other piston, assuming the pistons are all in phase with one another (which is true in the case of constant-depth liner samples for the frequencies considered in the NIT). Given that radiation impedance is simply being modeled as the free-space wavenumber multiplied by the mass-end correction term, one can simply add up the mass-end correction values due to a piston's self-radiation impedance and its mutual radiation impedance with every other piston. This is shown as

$$\delta_i = \sum_{j=1}^{N_c} \delta_{ij} \tag{8}$$

for the i^{th} chamber.

4.2 Method 1: Midline-Length Assumption

The simplest method for computing the chamber reactance is the midline-length assumption. Here it is assumed that the bent-chamber is unfolded to be a straight chamber with the same midline length. As mentioned earlier, this is a common prediction scheme among the community. An example of a midline for a 180° bend is defined in Fig. 7a (shown as a dashed line).

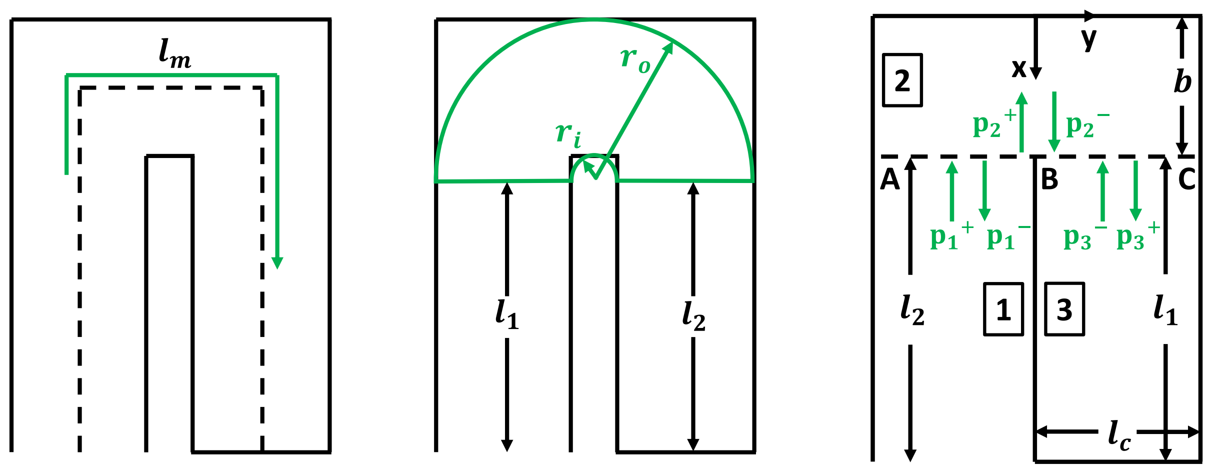

(a) Method 1 (b) Method 2 (c) Method 3

Figure 7: Problem setup for prediction methods 1–3 assuming a chamber bend angle of 180°. Method 1 is the midline-length assumption; method 2 is the Cummings correction for curved duct bends; method 3 is the Cummings prediction for 180° sharp duct bends.

The chamber reactance is then calculated assuming a straight chamber with no viscothermal losses, shown as

$$\chi_c = -\cot(kl_m). \tag{9}$$

4.3 Method 2: Cummings Correction for Curved Duct Bends

Cummings [2] computed the impedance of curved duct bends at arbitrary angles. Note here that the obvious advantage to this approach is the use of any bend angle, but the drawback is it assumes a curved duct bend and not a sharp duct bend that is more commonly used for bent-chamber liners, including the ones in this study. Hence, assumptions must be made about the geometry of each sample. Figure 7b shows the geometric assumptions made for the Cummings correction, using a chamber bend of 180° as an example. It is shown that the sharp bend is replaced by a curved bend, with the inner radius being equal to half the partition thickness. This is a similar approach to that assumed by Nark & Jones [8]. The Cummings correction approach also assumes a constant radius as the curve bends through the angle, so unfortunately chamber bend designs with a slot height other than the cross-sectional size of the chambers themselves cannot be predicted with this approach.

The Cummings correction method works by adding an effective length to the straight sections of the chamber to account for the bend. To accomplish this, an angular wavenumber is defined and computed using

$$J'_{k_\phi}(kr_i)Y'_{k_\phi}(kr_o) - J'_{k_\phi}(kr_o)Y'_{k_\phi}(kr_i) = 0, \tag{10}$$

where an iterative process must be used. For more information on how Eq. (10) is derived, please refer to Cummings [2]. Once the dimensionless angular wavenumber is computed, the effective chamber reactance can be solved using

$$\chi_c = -\cot\left[k\left(\psi\frac{k_\phi}{k} + l_1 + l_2\right)\right]. \tag{11}$$

Cummings [2] notes that for curved bends, the primary effect has less to do with the generation of higher-order modes, but rather simply a change in the propagation characteristics due to the bend. Therefore, simply correcting the midline length of the curved bend is a viable strategy. In short, it modifies the midline length of the bend by changing the propagation velocity, using the angular wavenumber instead of the free-space wavenumber.

Note that the l_1 and l_2 summation in Eq. (11) for these particular samples can be computed using

$$l_1 + l_2 = l_m - (l_c + t_p)\tan\left(\frac{\psi}{2}\right) \tag{12}$$

for $0 \leq \psi \leq \frac{\pi}{2}$, and

$$l_1 + l_2 = l_m - (l_c + t_p)\left[1 + \tan\left(\frac{\psi - \frac{\pi}{2}}{2}\right)\right] \tag{13}$$

for $\frac{\pi}{2} < \psi \leq \pi$. It is important to note again that various geometric assumptions are made in order to use this method, and one could make different assumptions and get different answers. This will be discussed later in the document.

4.4 Method 3: Cummings Prediction for 180° Sharp Duct Bends

Cummings [3] developed an impedance prediction scheme for 180° sharp, rectangular chamber bends*. This includes the ability to vary the slot height. To do this, an acoustic modal solution is developed, which will be shown in this section, but please refer to Cummings [3] for more details if needed. Figure 7c shows the coordinate system and problem setup for the prediction, where it should be noted that the analytical domain is broken out into three distinct sections. Note that the wavenumber in the z direction (out of the page) can be defined as zero throughout since there are no discontinuities present. Additionally, it is important to mention that this xy coordinate system is separate from the xy coordinate system used in the radiation impedance calculation. The acoustic pressure in each of the three sections may be described by an infinite summation of rectangular duct mode solutions. These are shown as

*This formulation is written in the $e^{-i\omega t}$ convention so as to preserve the original intent of the author. The reactance is then negated at the end to switch back to the $e^{i\omega t}$ convention to be in line with the other methods.

$$p_1(x,y) = \sum_{m=0}^{\infty} (P_{1,m}^{+} \mathrm{e}^{-ik_{1,m}x} + P_{1,m}^{-} \mathrm{e}^{ik_{1,m}x}) \cos\left(\frac{\pi m y}{l_c}\right), \tag{14}$$

$$p_2(x,y) = \sum_{m=0}^{\infty} P_{2,m} \cos(k_{2,m}x) \Gamma_m, \tag{15}$$

$$p_3(x,y) = \sum_{m=0}^{\infty} (P_{3,m}^{+} \mathrm{e}^{ik_{3,m}x} + P_{3,m}^{-} \mathrm{e}^{-ik_{3,m}x}) \cos\left(\frac{\pi m y}{l_c}\right), \tag{16}$$

where the axial wavenumbers are defined as

$$k_{i,m} = \sqrt{k^2 - \left(\frac{\pi m}{l_c}\right)^2}, \tag{17}$$

and the Γ_m term is defined as

$$\Gamma_m = \begin{cases} \cos\left(\frac{\pi m y}{2 l_c}\right) & m = 0, 2, ... \\ \sin\left(\frac{\pi m y}{2 l_c}\right) & m = 1, 3, ... \end{cases} \tag{18}$$

where it should be noted that this solution assumes an infinitely thin partition.

The bend in the chamber facilitates the need to account for a small number of higher-order modes. It was shown in Cummings [3] that a third-order solution provided the best impedance predictions, meaning that the acoustic pressure summation should go to $m = 3$ for section 2 and $m = 1$ for sections 1 and 3. It is important to note, however, that the needed solution order is partially reliant on both the geometry of the chambers as well as the frequencies of interest, so care should be taken here to properly choose the solution order based on the needed application. The intent of the prediction is to solve for the complex modal amplitudes, and a third-order solution would generate twelve unknowns. However, a variety of assumptions and boundary conditions can be used to reduce the number of unknowns.

As long as the cut-on frequency of the first higher order mode in sections 1 and 3 is significantly higher than the highest frequency of interest (which is true for the samples of interest), $P_{1,m}^{+}$ and $P_{3,m}^{-}$ for $m > 0$ are effectively zero. Additionally, the rigid termination at the end of section 3 means the particle velocity normal to the termination is zero, which implies that the acoustic pressure derivative as a function of x must also be zero at this location. Effectively this means $P_{3,0}^{-}$ can be expressed as a function of $P_{3,m}^{+}$. Finally, one can solve for modal amplitude ratios such that the acoustic pressures in each section can be set as a ratio of $P_{1,0}^{+}$. These assumptions and boundary conditions lower the number of unknowns to eight, meaning eight equations are needed.

One can use continuity of pressure and particle velocity at the boundaries of the sections to generate the equations. These are shown as

$$\int_{-l_c}^{0} \left(\frac{p_1}{P_{1,0}^{+}}\right) \cos\left(\frac{\pi s y}{l_c}\right) \, dy = \int_{-l_c}^{0} \left(\frac{p_2}{P_{1,0}^{+}}\right) \cos\left(\frac{\pi s y}{l_c}\right) \, dy, \tag{19}$$

$$\int_{-l_c}^{0} \frac{\partial}{\partial x} \left(\frac{p_1}{P_{1,0}^{+}}\right) \cos\left(\frac{\pi s y}{l_c}\right) \, dy = \int_{-l_c}^{0} \frac{\partial}{\partial x} \left(\frac{p_2}{P_{1,0}^{+}}\right) \cos\left(\frac{\pi s y}{l_c}\right) \, dy, \tag{20}$$

$$\int_0^{l_c} \left(\frac{p_3}{P_{1,0}^+}\right) \cos\left(\frac{\pi s y}{l_c}\right)\, dy = \int_0^{l_c} \left(\frac{p_2}{P_{1,0}^+}\right) \cos\left(\frac{\pi s y}{l_c}\right)\, dy, \tag{21}$$

$$\int_0^{l_c} \frac{\partial}{\partial x} \left(\frac{p_3}{P_{1,0}^+}\right) \cos\left(\frac{\pi s y}{l_c}\right)\, dy = \int_0^{l_c} \frac{\partial}{\partial x} \left(\frac{p_2}{P_{1,0}^+}\right) \cos\left(\frac{\pi s y}{l_c}\right)\, dy, \tag{22}$$

where pressure and particle velocity terms are multiplied by independent functions and integrated over the boundaries.

If one sets $s = (0, 1)$, there are eight total equations that can be used to solve for the unknowns. For the purposes of surface impedance, only the reflected to incident pressure ratio in section 1 for $m = 0$ is of interest, as this is the complex reflection coefficient that can be used to calculate the surface impedance. The final calculation for the chamber reactance is computed via

$$\chi_c = -\Im\left\{\frac{1 + Re^{i2k(l_2+b+t_p)}}{1 - Re^{i2k(l_2+b+t_p)}}\right\}, \tag{23}$$

where this is simply the imaginary part of the acoustic pressure to acoustic velocity ratio at $m = 0$ and at the surface of interest. The reflection coefficient is defined as

$$R = \frac{P_{1,0}^-}{P_{1,0}^+}. \tag{24}$$

As mentioned previously, this formulation assumes an infinitely thin partition. The samples of interest in this study have a partition thickness of $0.1''$, so it cannot be assumed negligible. Since the partition thickness adds a small amount to the total midline length of the chamber, it is reasoned that a very rough approximation to account for this in the Cummings formulation is to add the partition thickness to the $l_2 + b$ length in the impedance calculation (Eq. (23)). Do note though that other options should be explored in the future to more accurately account for the physics, as for instance the cut-on behavior changes in the bend when the partition thickness is finite.

4.5 Method 4: Helmholtz Equation via Finite Element Method

Lastly, one can also compute the surface impedance of these samples via Actran TM [14]. Actran is a commercially available and general-purpose finite element program for modeling noise propagation and radiation. It is comprised of two high-level components: Actran TM and Actran DGM. Actran TM is used in this study, which solves the convected Helmholtz equation in potential flow.

In order to compute the impedance, a given sample is explicitly modeled in the NIT environment. This means the radiation impedance is already accounted for, and therefore an added term for the radiation impedance does not need to be used, unlike the other methods. The two-microphone method [21, 22] is replicated by placing virtual microphones at the same locations as the centers of the measurement microphones in the NIT. It is important to note that the data captured by the microphones in the Actran simulation are interpolated values at discrete points, whereas in the NIT experimental measurement, the data are averaged values over the microphone surfaces ($0.25''$ diameter microphones). This particular two-microphone method algorithm does not include any viscothermal losses in the duct to be in line with the Actran assumptions, where it is assumed that both the NIT and the sample chambers experience no viscothermal losses.

Figure 8 shows the typical computational setup involved. Please note that the full NIT is not being modeled but rather a section of it. This is sufficient for modeling purposes, as the NIT physical system has a longer length to ensure a pure plane wave impinges upon the sample surface. Correspondingly, the computational domain assumes plane-wave propagation.

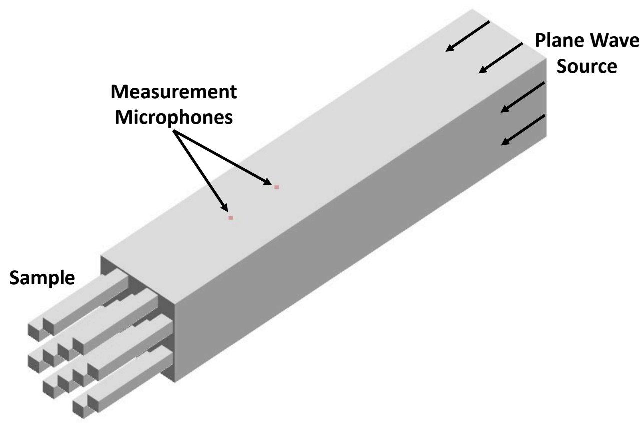

Figure 8: Actran computational setup using BC-1 as an example. The red dots are the virtual measurement microphones.

5 Experimental Results

Figure 9 shows the normalized impedance of the various samples at a source level of 120 dB. Note again that the data were acquired from 400–3000 Hz using the swept-sine source, meaning the data resolution is close to 5 Hz. All data shown in this report do not show anything lower than 500 Hz though, as most key features pointed out in this report do not occur at frequencies between 400–500 Hz. BC-5, BC-6, BC-10, and BC-11 are excluded from Fig. 9 in order to demonstrate the effect of bend angle only, of course noting that BC-9's total midline length is 0.03″ smaller than the other samples. Also note that since these samples only include open chambers and no facesheet, the measured differences between data acquired with source levels of 120 and 140 dB are minimal.

As expected, resistance values are small since viscothermal losses are fairly low when the chamber cross-sections are of a reasonably large size. Resistive differences between cases are nearly negligible with the only real differences occurring near antiresonance, which is simply due to a change in reactance behavior. It is anticipated that resistive differences between cases may have been greater with smaller chamber cross-sections. This should be explored in more detail in the future. The reactance data shows a gradual lowering of values as the chamber bend angle increases. Diminishing reactance produces a shift to higher resonant (and antiresonant) frequencies. Only resonance is captured within the frequency range examined in this study.

Table 2 shows the extracted resonant frequencies for every sample tested at 120 and 140 dB. Again, it is clear from Table 2 that extracted resonant frequencies between the two SPL cases are virtually the same. There is a shift of almost 140 Hz between BC-1 and BC-9, noting also that with the exception of BC-2, the resonant frequency continues to increase as the bend angles of the samples increase. It is estimated that the 0.03″ difference in total midline length for BC-9 accounts

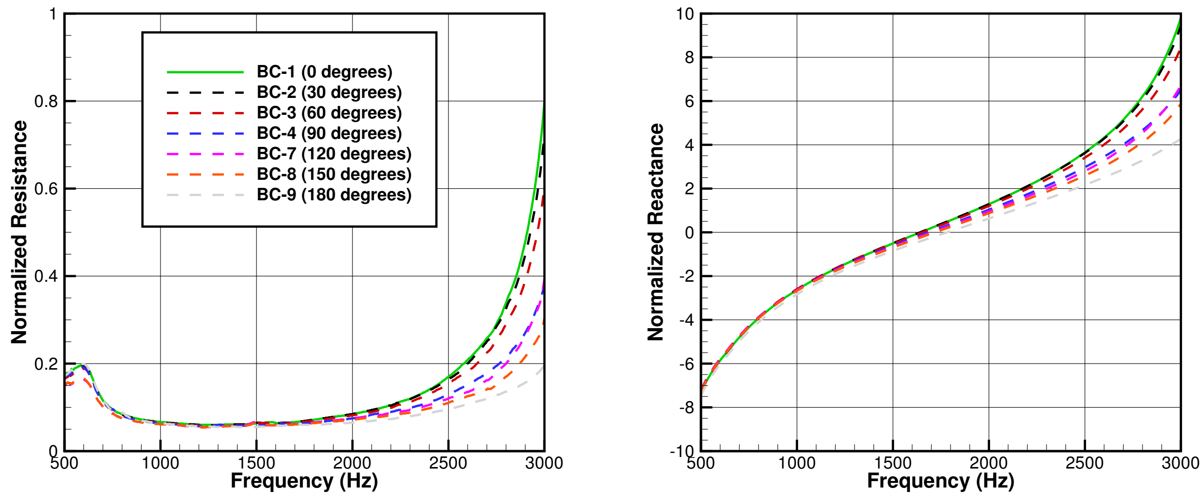

(a) Normalized resistance.

(b) Normalized reactance.

Figure 9: Normalized impedance vs. frequency (Hz) for various chamber bends at 120 dB. Resistance differences are minor other than near antiresonance. Reactance differences show a gradual shift in resonance to higher frequencies for increasing bend angle.

for roughly 25 Hz of its shift, so this would indicate roughly 115 Hz of the shift from BC-1 to BC-9 is due to the bend angle alone. Overall, these data show that, at least for the chamber diameters and frequencies assessed in this study, equivalent midline length chambers do not behave the same way when different bend angles are present.

Table 2: Resonant frequencies for each sample.

Sample Name	120 dB	140 dB
BC-1	1644.1 Hz	1643.5 Hz
BC-2	1641.5 Hz	1640.8 Hz
BC-3	1653.8 Hz	1652.7 Hz
BC-4	1684.2 Hz	1683.2 Hz
BC-5	1666.2 Hz	1665.4 Hz
BC-6	1707.4 Hz	1705.9 Hz
BC-7	1702.0 Hz	1702.0 Hz
BC-8	1719.2 Hz	1719.4 Hz
BC-9	1781.7 Hz	1780.6 Hz
BC-10	1967.6 Hz	1966.7 Hz
BC-11	1608.1 Hz	1604.9 Hz

There is recent interest in adjusting the slot height to modify the resonant frequency of the chamber. As mentioned earlier, a detailed study of this was already performed in Jones et al. [18], but for the current study, it was desired to have a few slot-adjusted samples for modeling purposes. Figure 10a shows the effect of varying the slot height using samples BC-9, BC-10, and BC-11. In theory, lowering the slot height should increase the midline length of the chamber and lower the resonant frequency. The opposite would then be true for raising the slot height. Figure 10a does indeed show this to be the case, as significant differences in reactance are achieved. Table 2 shows there is a 350+ Hz shift in resonant frequency between the large (BC-10) and small (BC-11) slot. Jones et al. [18] significantly widened the slot-height variation compared to this study, and the resonant frequencies varied even more strongly. Continued work should be pursued on slot-height variation.

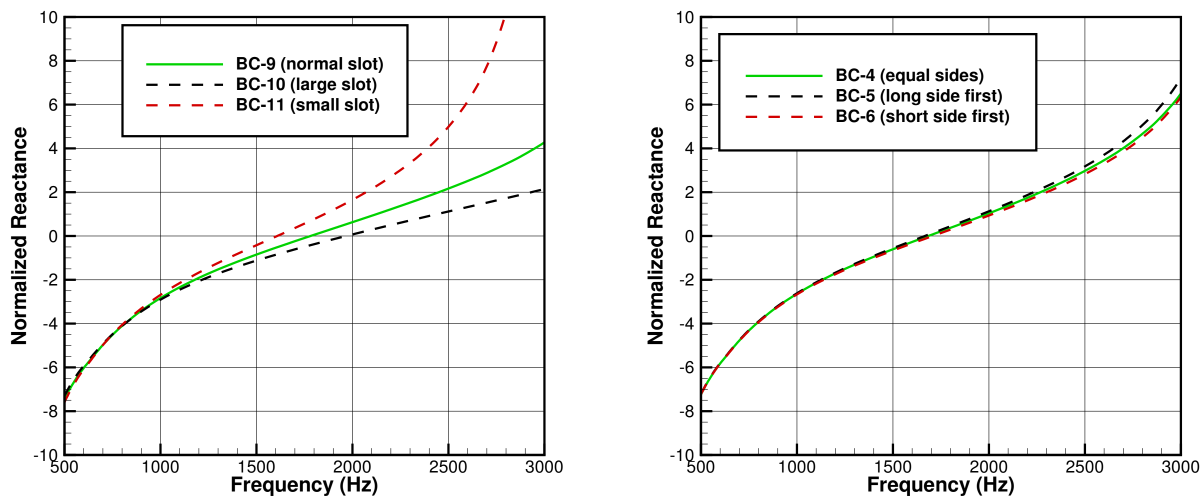

(a) Slot-height variation.

(b) Side-length variance.

Figure 10: Normalized reactance vs. frequency (Hz) showing the effect of slot height and varying the side lengths on chamber bends. Significant resonance shifts can be achieved by varying the slot height. However, very little differences are observed with side-length variance, although higher frequencies may show larger differences.

Samples BC-5 and BC-6 are meant to assess the effect of adjusting the long and short side lengths of a given bent chamber. As mentioned previously, Sugimoto et al. [13] suggested that at higher frequencies, the bent chamber will act more like a straight chamber that terminates at the wall of the bend, indicating that maintaining the midline length but adjusting where the bend is located could have an impact on the impedance. Figure 10b shows very little difference due to the placement of the bend. However, the expected trends are present. The sample with the longer side closer to the liner surface (BC-5) produces reactance data that is slightly higher than the equivalent side sample (BC-4). Comparatively, the sample with the shorter side closer to the liner surface (BC-6) has the lowest reactance data. Referring once again to Table 2, one can see that the resonant frequency shifts about 40 Hz between BC-5 and BC-6. However, to truly see the impact of the bend placement, it is likely that the samples should be retested at higher frequencies.

6 Prediction Results

The mass-end correction terms for the radiation impedance of each chamber are first calculated. Note that every sample has the same array of terms, since all samples have the same surface layout and contain chambers with the same cross-sectional geometry. Additionally, each chamber is identical for a given sample, so all chambers are radiating noise in phase with one another. Figure 11 shows the influence of including the radiation effect within the impedance prediction process for the baseline case with no bend (BC-1). Although the effect is small, there is a clear improvement in the prediction. With the prediction for sample BC-1 verified, these same mass-end correction terms are subsequently used for the predictions of the remaining samples. Figure 12 shows the impedance predictions of the first three methods for all samples except BC-5 and BC-6. Note that not all methods are applicable for every sample. The following sections will comment on the applicability of each method.

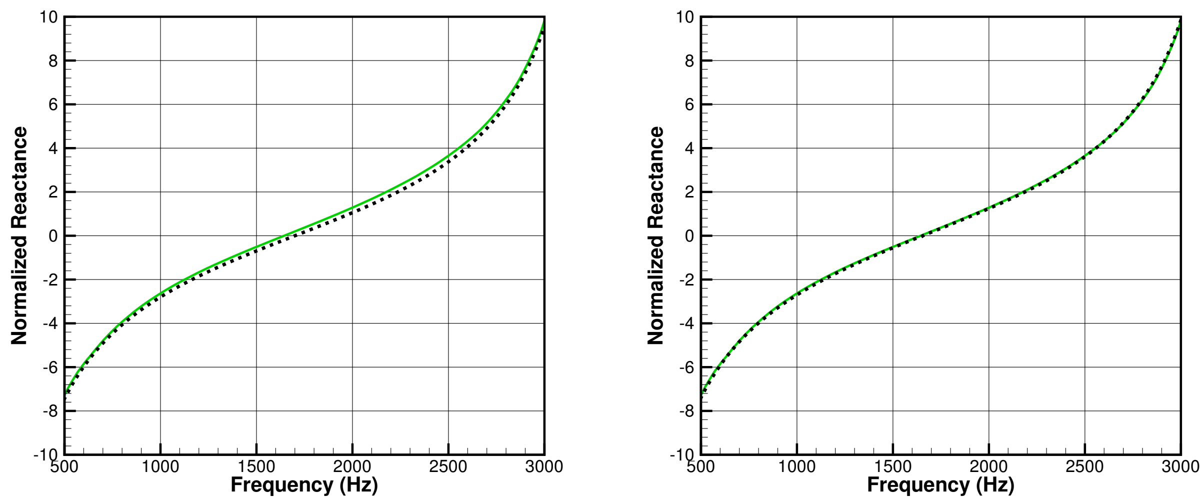

(a) No radiation reactance included.

(b) Radiation reactance included.

Figure 11: BC-1 reactance prediction showing the influence of the radiation effect. Solid green line is experimental data; dotted black line is prediction.

6.1 Method 1: Midline-Length Assumption

It is clear from Fig. 12 that the midline-length assumption generally does a good job at predicting the impedance up until a certain frequency, at which point the prediction quality deteriorates. This is in line with expectations, as the midline-length assumption will break down as kl_c values go up. It is also important to note that the frequency at which the prediction starts to worsen lowers as the bend angle goes up. It stands to reason that a critical kl_c value exists for each sample that defines this break-down point.

To identify the critical kl_c values, it will be assumed that the prediction breaks down when the difference between the prediction and experimental data differs by an absolute value of 0.25. Although a prediction error of 0.25 is typically very good, one would expect a very accurate prediction for open chambers without a facesheet. Figure 13 shows the critical kl_c values for a number of the samples (BC-2, BC-3, BC-4, BC-7, BC-8, and BC-9). BC-10 and BC-11 are excluded from this exercise as they are not constant cross-section bends. There has also been a logarithmic curve fit added to the plot, which seems reasonable given the critical frequency should approach an infinite value as the bend angle approaches 0°, as long as the first cut-on frequency of the chamber is suf-

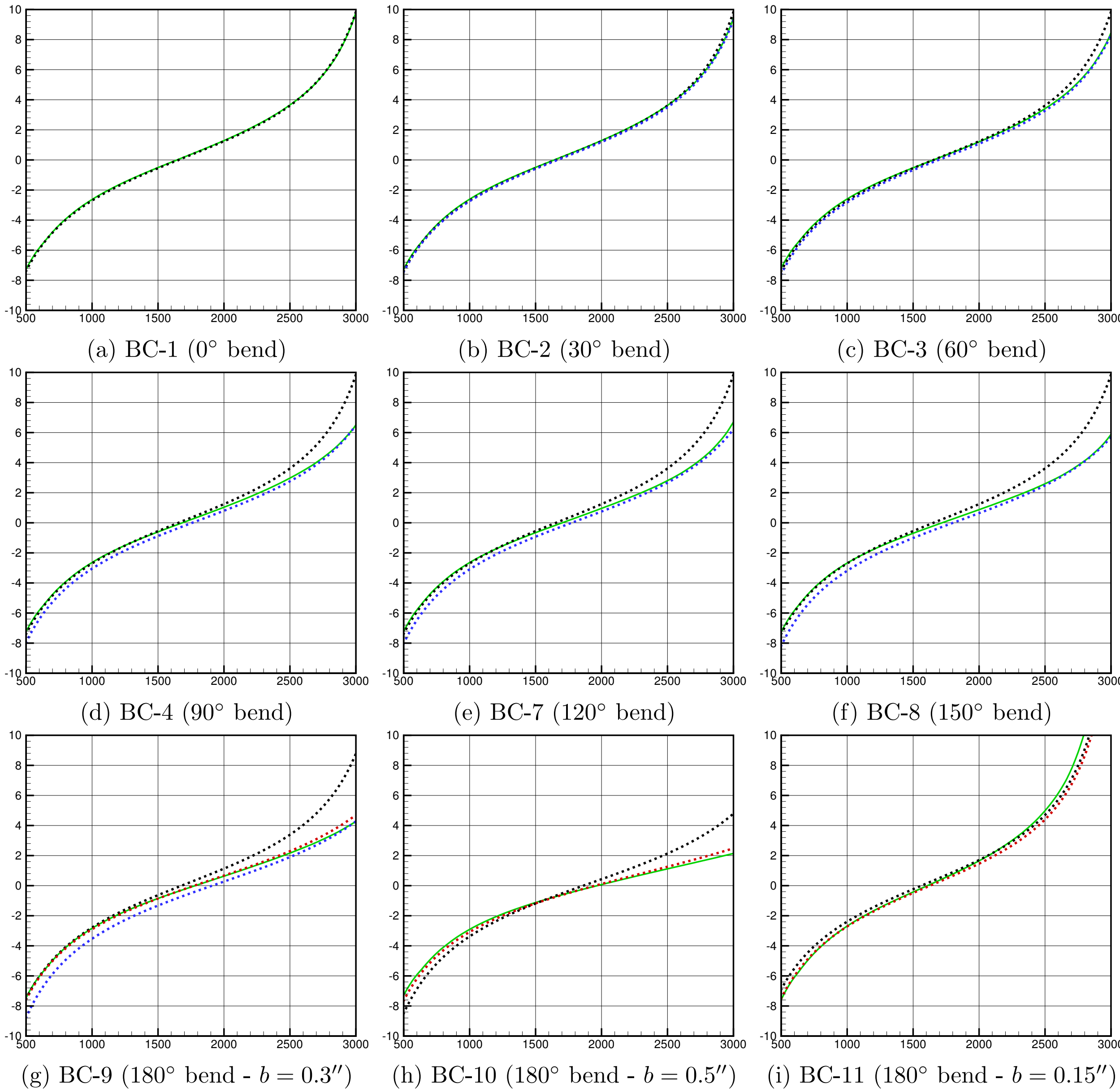

(a) BC-1 (0° bend) (b) BC-2 (30° bend) (c) BC-3 (60° bend)

(d) BC-4 (90° bend) (e) BC-7 (120° bend) (f) BC-8 (150° bend)

(g) BC-9 (180° bend - $b = 0.3''$) (h) BC-10 (180° bend - $b = 0.5''$) (i) BC-11 (180° bend - $b = 0.15''$)

Figure 12: Normalized reactance vs. frequency (Hz) utilizing prediction method 1: midline-length assumption, method 2: Cummings correction for curved duct bends, and method 3: Cummings prediction for 180° sharp duct bends. Solid green lines are experimental data; dotted black lines are method 1; dotted blue lines are method 2; dotted red lines are method 3.

ficiently higher than the frequency of interest. As one can see, the critical frequency drops as the bend angle increases, and it appears that this trend for increasing bend angle can be reasonably predicted by a logarithmic curve fit. To further validate this claim, one would need to look at samples with additional bend angles and chamber diameters tested at a wider range of frequencies. This is planned for future studies.

For the test samples in this study, the critical kl_c values are in the 0.2–0.4 range. These values appear reasonable as research that has successfully used the midline-length assumption [9, 11, 12] typically looked at values below 0.1. In short, the midline-length assumption does an excellent job at predicting bent-chamber impedance up to the critical frequencies. Beyond that, the prediction quickly deteriorates. It is also important to comment on the applicability of using the midline-length assumption for a chamber bend with a variable cross-section, i.e., samples BC-10 and BC-11. It would appear that the assumption works better when the slot height is smaller (see Fig. 12 for BC-11), and this intuitively makes sense, as the one-dimensional propagation assumption should hold better.

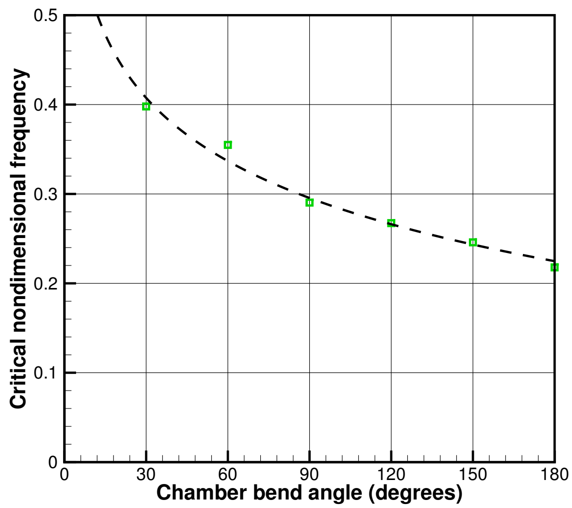

Figure 13: Critical kl_c vs. chamber bend angle (degrees). Green dots are experimental data; black dashed line is a logarithmic curve fit.

6.2 Method 2: Cummings Correction for Curved Duct Bends

Figure 12 also shows the accuracy of Cummings correction for curved duct bends. It can be seen that the trends of this method are opposite of the midline-length assumption: the prediction seems to become more accurate at higher frequencies. Due to the increased accuracy at higher frequencies, one would anticipate it does a better job at predicting the antiresonance compared to the midline-length assumption. However, the antiresonance is not quite captured in the measured results for these samples due to the frequency limitation of the NIT. Samples should be retested at higher frequencies to gain a better understanding of the prediction accuracy, and this can be accomplished through the NASA High Intensity Modal Impedance Tube (HIMIT) [30], where frequencies up to 6000 Hz can be studied. It would appear though that the midline-length assumption is arguably more accurate at predicting the resonant frequency. Given the trends of methods 1 and 2, it is possible that one could use a bridging function around the critical kl_c value to merge the two results and yield a more accurate final answer.

However, one must take great care in making assumptions on the accuracy of method 2. As mentioned earlier, the results of this method are highly dependent on the geometric assumptions being made. For example, this study briefly approached this method another way. One can see in

Fig. 7b that under the current assumption, the curved bend replaces the sharp bend in a manner that the curved bend has a smaller midline length. This would at least partially explain why the Cummings correction is producing more inaccuracies at lower frequencies. To help account for this, the Cummings correction was used to replace the sharp bend with a curved bend of the same midline length and chamber cross-section. Using this approach, the lower-frequency accuracy was significantly improved while the higher-frequency accuracy deteriorated, to the point where it was only slightly better than the midline-length assumption. Hence, it is thought that the Cummings correction is an improvement to the midline-length assumption. However, there is enough evidence to also suggest that assuming a curved bend instead of a sharp bend is simply not capturing the physics properly. This is why the second prediction method of Cummings [3] was also assessed.

6.3 Method 3: Cummings Prediction for 180° Sharp Duct Bends

This method is used to predict the impedance of all 180° chamber bend samples: BC-9, BC-10, and BC-11. This includes the approximation to account for the partition thickness. One can see in Fig. 12 that this method produces accurate results across nearly the entire frequency range for all three samples. It is particularly of value to see its accuracy for slot-height variation. It outperforms the other methods in every case except for the higher frequencies using BC-11, where the midline-length assumption is actually slightly better. As it is still a fairly quick model in terms of computational time, one should strongly consider method 3 for 180° chamber bend predictions, even potentially in design studies. It would also be of interest to apply the model to other test cases, particularly the work conducted in Jones et al. [18], to gain more insight into the accuracy.

6.4 Method 4: Helmholtz Equation via Finite Element Method

The results of using Actran TM are shown in Fig. 14, where a solution is generated every 100 Hz to keep the computational cost low (less than ten seconds per frequency). Note that for the sake of brevity, only five samples are considered. As expected, one can see great accuracy produced by this method. Typically the main drawback of a method such as this is computational time, as it makes it more impractical to integrate into a design study. However, recent interest and test cases have been conducted on shape optimization in Actran TM [31], where the acoustic liner computational grid within the process is morphed per iteration until an objective function is met. This process is still early in development, but it is a potential opportunity to more accurately design bent-chamber liners. Additionally, the Actran predictions are sufficiently accurate that one could potentially perform a numerical study with Actran using a variety of test samples for evaluation of the other prediction methods.

7 Summary and Future Work

A study was conducted to both understand experimental trends as well as assess existing prediction schemes for bent-chamber liners. Every liner consisted of a 5×5 array of $0.3'' \times 0.3''$ square chambers with no facesheet. These samples were tested in a normal-incidence environment at SPL levels of 120 and 140 dB at frequencies from 400–3000 Hz. A total of eleven samples were tested with varying bend angles, bend locations, and slot height. For the test samples considered in this study, chambers with an equivalent midline length but differing bend angles produced different impedance data, namely a lowering in the reactance, which resulted in higher resonant frequencies

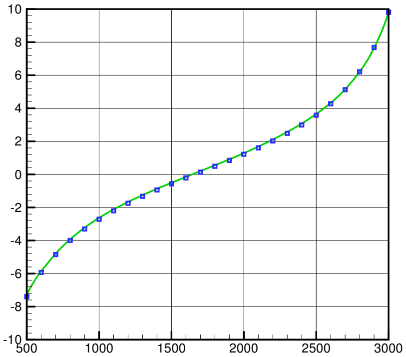

(a) BC-1 (0° bend)

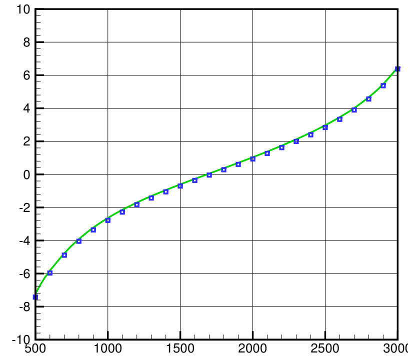

(b) BC-4 (90° bend)

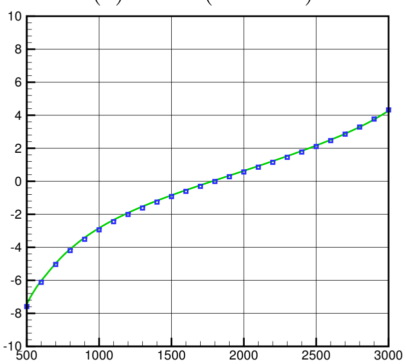

(c) BC-9 (180° bend - $b = 0.3''$)

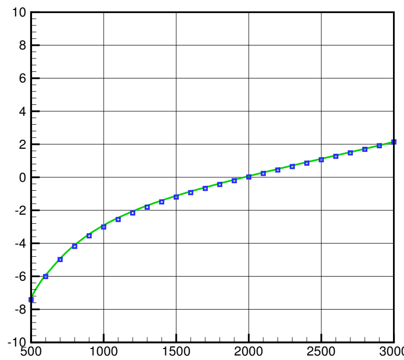

(d) BC-10 (180° bend - $b = 0.5''$)

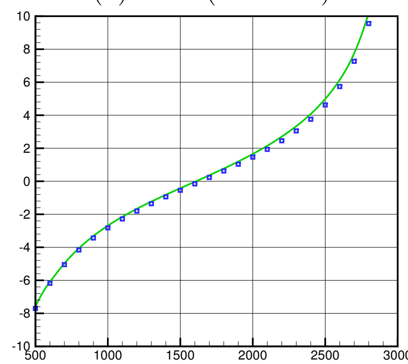

(e) BC-11 (180° bend - $b = 0.15''$)

Figure 14: Normalized reactance vs. frequency (Hz) utilizing Actran TM for 0°, 90°, and 180° chamber bend predictions. Solid green lines are experimental data; blue squares are Actran predictions.

for increasing bend angle. Resistance changes were small for the chamber cross-sections considered in this study.

Four impedance prediction methods were described and used in this study: (1) midline-length assumption, (2) Cummings correction for curved duct bends, (3) Cummings prediction for 180° sharp duct bends, and (4) Helmholtz equation via finite element method. A radiation impedance model was included in the classical modeling approaches and resulted in a minor but improved prediction. A midline-length assumption performed well at predicting the impedance of bent-chamber liners up to a critical frequency, at which point deviation occurred. Likely, a one-dimensional propagation assumption begins to break down at this point. Extraction of this critical frequency (more specifically the nondimensional frequency kl_c) appears to scale logarithmically with bend angle, i.e., the higher the bend angle, the lower the critical frequency.

The Cummings correction for curved duct bends produced marginally better results than the midline-length assumption, but it is highly dependent on the geometric assumptions that are used. The physics of curved duct bends are simply different than sharp duct bends, so likely no manipulation of the model will be the answer for sharp duct bends. The Cummings prediction for 180° sharp duct bends (with an added correction for finite partition thickness) produced quality predictions, at least for the samples considered in this study. Finally, a finite element method using the Helmholtz equation (Actran TM in this study) produced the best results. This is the only method that can accurately model the impedance for every sample in this study.

There is a large amount of follow-on work that should be explored to verify and expand on the findings in this paper. The samples in this study should be retested in the NASA HIMIT to obtain data at higher frequencies. This would help capture the antiresonant spikes and provide further clarity on the accuracy of each model. It would also help clarify the differences between samples having the same total midline length but differing lengths on either side of the bend (BC-5 and BC-6). Furthermore, additional samples should be 3D-printed and tested. Variations in the samples should include different chamber diameters, depths, bend angles, and partition thicknesses. This would improve the understanding of the critical nondimensional frequency (kl_c) and how that relates to the midline-length assumption, since this is the prediction method that most people in the community use.

Further understanding on the accuracy and implementation of the Cummings prediction for 180° sharp duct bends is also warranted. This could be a valuable option for chamber bend designs in the future, especially when slot-height variation is considered. A reexamination of the formulations is also of value to see if the problem setup can be extended more generally for chamber bends. Finally, shape optimization within Actran TM should be explored further, as it may be the best way to design bent-chamber liners in the future.

References

1. W. Rostafinski, "Monograph on Propagation of Sound Waves in Curved Ducts," NASA RP-1248, 1991.

2. A. Cummings, "Sound Transmission in Curved Duct Bends," *Journal of Sound and Vibration*, vol. 35, no. 4, pp. 451–477, 1974.

3. A. Cummings, "Sound Transmission in 180° Duct Bends of Rectangular Section," *Journal of Sound and Vibration*, vol. 41, no. 3, pp. 321–334, 1975.

4. A. Cummings, "Sound Transmission in a Folded Annular Duct," *Journal of Sound and Vibration*, vol. 41, no. 3, pp. 375–379, 1975.

5. D. Sawdy and R. Beckemeyer, "Bandwidth Attenuation with a Folded Cavity Liner in a Circular Flow Duct," *AIAA Journal*, vol. 18, no. 7, pp. 766–773, 1980.

6. J. Yu and E. Chien, "Folding Cavity Acoustic Liner for Combustion Noise Reduction," AIAA Paper 2006-2681, 2006.

7. M. Martinez, "Determination of Combustor Noise from a Modern Regional Aircraft Turbofan Engine," AIAA Paper 2006-2676, 2006.

8. D. Nark and M. Jones, "A Fundamental Study of Bifurcation Acoustic Treatment Effects on Aft-Fan Engine Noise," AIAA Paper 2023-3345, 2023.

9. D. Nark, M. Jones, J. Kreitzman, and B. Schuster, "Bypass Duct Acoustic Liner Design with and without Bifurcation Effects," AIAA Paper 2024-3250, 2024.

10. T. Parrott, M. Jones, and B. Homeijer, "Effect of Resonator Axis Skew on Normal Incidence Impedance," AIAA Paper 2003-3307, 2003.

11. B. Howerton and T. Parrott, "Validation of an Acoustic Impedance Prediction Model for Skewed Resonators," AIAA Paper 2009-3143, 2009.

12. J. Kreitzman, "Conceptual Design and Validation of a Bent-Perforation-Path Acoustic Liner," NASA/TM-20230018517, 2024.

13. R. Sugimoto, P. Murray, and R. Astley, "Folded cavity liners for turbofan engine intakes," AIAA Paper 2012-2291, 2012.

14. "Actran 2022 User's Guide Vol. 1 – Installation, Operations, Theory, and Utilities," 2022.

15. M. Marinova, M. Jones, and N. Schiller, "Evaluation of Packing_3D Code for Design of Variable-Depth, Bent-Chamber Acoustic Liners," NASA/TM–2020–220560, 2020.

16. A. Chambers, J. Manimala, and M. Jones, "Design and Optimization of 3D Folded-Core Acoustic Liners for Enhanced Low-Frequency Performance," *AIAA Journal*, vol. 58, no. 1, pp. 206–218, 2020.

17. S. Palani, P. Murray, A. McAlpine, D. Sasaki, and C. Richter, "Slanted septum and multiple folded cavity liners for broadband sound absorption," *International Journal of Aeroacoustics*, vol. 20, no. 5–7, pp. 633–661, 2021.

18. M. Jones, D. Nark, and N. Schiller, "Evaluation of Variable-Depth Liners with Slotted Cores," AIAA Paper 2022-2823, 2022.

19. M. Jones, F. Simon, and R. Roncen, "Broadband and Low-Frequency Acoustic Liner Investigations at NASA and ONERA," *AIAA Journal*, vol. 60, no. 4, pp. 2481–2500, 2022.

20. M. Jones, W. Watson, D. Nark, B. Howerton, and M. Brown, "A Review of Acoustic Liner Experimental Characterization at NASA Langley," NASA TP-2020-220583, 2020.

21. J. Chung and D. Blaser, "Transfer function method of measuring in-duct acoustic properties: I. theory," *The Journal of the Acoustical Society of America*, vol. 68, pp. 907–921, 1980.

22. M. Jones and P. Stiede, "Comparison of methods for determining specific acoustic impedance," *The Journal of the Acoustical Society of America*, vol. 101, no. 5, pp. 2694–2704, 1997.

23. J. Kreitzman and M. Jones, "Influence of Source Type on Acoustic Liner Impedance in No Flow," AIAA Paper 2024-3249, 2024.

24. M. Jones and T. Parrott, "Evaluation of a Multi-Point Method For Determining Acoustic Impedance," *Mechanical Systems and Signal Processing*, vol. 3, no. 1, pp. 15–35, 1989.

25. T. Parrott and M. Jones, "Assessment of NASA's Aircraft Noise Capability, Chapter 6: Uncertainty in Acoustic Liner Impedance Measurement and Prediction," NASA TP 2012-215653, 2012.

26. N. Schiller and M. Jones, "Smeared Impedance Model for Variable Depth Liners," AIAA Paper 2018-3774, 2018.

27. U. Ingard, "On the Theory and Design of Acoustic Resonators," *The Journal of the Acoustical Society of America*, vol. 25, no. 6, pp. 1037–1061, 1953.

28. J.-G. Ih, "On the Inertial End Correction of Resonators," *Acta Acustica united with Acustica*, vol. 78, pp. 1–15, 1993.

29. R. Pritchard, "Mutual Acoustic Impedance between Radiators in an Infinite Rigid Plane," *The Journal of the Acoustical Society of America*, vol. 32, no. 6, pp. 730–737, 1960.

30. M. Jones, A. Carr, D. Nark, and L. Becker, "Implementation of the NASA High Intensity Modal Impedance Tube," NASA TM-20220017773, 2022.

31. J. Kreitzman, "Acoustic Liner Design Utilizing Propagation Solvers of Varying Fidelity," Presented at the 2023 NASA Langley Acoustic Liner Workshop, 2023.

REPORT DOCUMENTATION PAGE	Form Approved OMB No. 0704–0188

1. REPORT DATE *(DD-MM-YYYY)*	2. REPORT TYPE	3. DATES COVERED *(From - To)*
01-11-2024	Technical Memorandum	

4. TITLE AND SUBTITLE	
An Experimental and Predictive Study of Bent-Chamber Acoustic Liners	5a. CONTRACT NUMBER
	5b. GRANT NUMBER
	5c. PROGRAM ELEMENT NUMBER
6. AUTHOR(S)	5d. PROJECT NUMBER
Jordan Kreitzman and Michael G. Jones	5e. TASK NUMBER
	5f. WORK UNIT NUMBER

7. PERFORMING ORGANIZATION NAME(S) AND ADDRESS(ES)	8. PERFORMING ORGANIZATION REPORT NUMBER
NASA Langley Research Center Hampton, Virginia 23681-2199	12456
9. SPONSORING/MONITORING AGENCY NAME(S) AND ADDRESS(ES)	**10. SPONSOR/MONITOR'S ACRONYM(S)**
National Aeronautics and Space Administration Washington, DC 20546-0001	NASA
	11. SPONSOR/MONITOR'S REPORT NUMBER(S)
	NASA/TM–20240014376

12. DISTRIBUTION/AVAILABILITY STATEMENT
Unclassified-Unlimited
Subject Category 64
Availability: NASA STI Program (757) 864-9658

13. SUPPLEMENTARY NOTES
An electronic version can be found at http://ntrs.nasa.gov.

14. ABSTRACT
Acoustic liner samples with rectangular, sharp chamber bends are 3D-printed and tested in the NASA Normal Incidence Tube. The angle of the bend is varied from 0° to 180°. Four different methods are used to predict the impedance behavior of these samples: (1) midline-length assumption, (2) Cummings correction for curved duct bends, (3) Cummings prediction for 180° sharp duct bends, and (4) Helmholtz equation via finite element method. Trends in the experimental data are discussed, predictions are compared to the experimental data, and recommendations are made on prediction method usage. Follow-on work is suggested, including capturing additional test points at higher frequencies and with different chamber geometries. Future modeling strategies are also briefly described.

15. SUBJECT TERMS
acoustic, liner, impedance, bent, chamber

16. SECURITY CLASSIFICATION OF:			17. LIMITATION OF ABSTRACT	18. NUMBER OF PAGES	19a. NAME OF RESPONSIBLE PERSON
a. REPORT	b. ABSTRACT	c. THIS PAGE			STI Information Desk (help@sti.nasa.gov)
					19b. TELEPHONE NUMBER *(Include area code)*
U	U	U	UU	32	(757) 864-9658

Standard Form 298 (Rev. 8/98)
Prescribed by ANSI Std. Z39.18